Effect of Mn content on physical properties of CeO_x–MnO_y support and BaO–CeO_x–MnO_y catalysts for direct NO decomposition

Won-Jong HONG [a], Shinji IWAMOTO [b], Saburo HOSOKAWA [a], Kenji WADA [a],

Hiroyoshi KANAI [a], Masashi INOUE [a,*]

[a] Department of Energy and Hydrocarbon Chemistry

Graduate School of Engineering, Kyoto University, Katsura, Kyoto, 615-8510, JAPAN

[b] Department of Chemistry and Chemical Biology,

Graduate School of Engineering, Gunma University, Tenjin, Kiryu 376-8515, JAPAN

[*] Corresponding author

Tel.: +81-75-383-2478

fax: +81-75-383-2479.

E-mail address: inoue@scl.kyoto-u.ac.jp (M. Inoue)

ABSTRACT

A series of manganese–cerium mixed oxides were prepared by a glycothermal method, and the NO decomposition activities of the Ba-loaded Ce–Mn oxides were examined. Among the catalysts examined, the highest NO conversion was obtained on the BaO/Ce–Mn oxide catalyst with a Mn/(Ce+Mn) ratio of 0.25. The X-ray diffraction and Raman analyses indicated the formation of Ce–Mn oxide solid solutions with a cubic fluorite structure. The electron spin resonance analysis indicated the presence of paramagnetic Mn^{2+} species in the composite catalysts. Incorporation of Mn^{2+} in the fluorite structure of CeO_2 causes an increase in the concentration of oxygen vacancies, which play an important role in the NO decomposition activity of the catalysts. The catalysts were also characterized by X-ray photoelectron spectroscopy and temperature-programmed reduction techniques. Based on the results obtained, the relationship between the physical properties of the catalysts and their NO decomposition activities was discussed.

Keywords: CeO_2, Ce–Mn mixed oxide, Direct NO decomposition, Oxygen vacancy

1. Introduction

Since the emission of nitrogen oxides (NO_x) causes severe environmental problems, effective methods to decrease NO_x concentration in emissions have been sought. Several practical NO_x emission control technologies such as three-way catalysts for gasoline-fueled vehicles, NO_x storage–reduction (NSR) systems for lean-burn engines, and selective catalytic reduction (SCR) processes for large-scale combustion facilities are now applied; however, there is still a great research interest for the development of novel and more efficient deNO_x methods. Among various deNO_x strategies, direct decomposition of NO ($NO \rightarrow 1/2O_2 + 1/2N_2$) is most desirable to remove NO_x from exhausts because this reaction is thermodynamically favorable and does not need any reductants such as NH_3, H_2, CO, or hydrocarbons.

A number of catalysts have been examined for this reaction, and several types of catalysts such as precious metals [1–4], ion-exchanged [5–8] or metal-loaded [9] zeolites, single component metal oxides [6,10,11], alkali- or alkaline earth-promoted metal oxides [12–14], and perovskites [15–20] have been found to be effective. Recently, C-type cubic rare earth oxides [21,22] and Ba/Ba-Y-O [23] were also reported to be active for this reaction. We found that Ba–Ce–Co mixed oxides prepared by a polymerized complex method showed high activities [24]. In order to investigate the

nature of the active sites of the catalysts, Ba catalysts supported on Co_3O_4 and CeO_2 were examined, and it was found that the NO conversion was correlated to the number of the basic sites [25]. An addition of second component to CeO_2 was examined and it was found that the Ba catalysts supported on the Ce–Mn mixed oxides [26] and on Ce–Fe mixed oxides [27] showed significantly high activities for this reaction.

Cerium oxide and CeO_2-containing materials have attracted much attention as catalyst as well as structural and electronic promoters for heterogeneous catalysts [28]. Some cerium–transition metal mixed oxides have large numbers of surface and bulk oxygen vacancies and, thus, possess improved oxygen storage capacities, and favorable redox properties were attained by these mixed oxides. Among numerous cerium-based mixed oxide systems, MnO_x–CeO_2 catalysts are known to be remarkably active in the oxidation of ethanol [29], formaldehyde [30], and phenol [31], as well as in the SCR of NO with NH_3 [32] . Machida et al. reported an excellent NO_x sorbability of the MnO_x–CeO_2 system at low temperatures [33].

In this study, the Ba-loaded Ce–Mn mixed oxides were characterized, and the correlation between the properties of the catalysts and their NO decomposition activities is discussed.

2. Experimental

2.1. Preparation of the catalysts

Cerium–manganese mixed oxides (designated as Ce–Mn(*x*), where *x* is the Mn/(Ce+Mn) molar ratio) were prepared by the glycothermal method. Appropriate amounts of $Ce(CH_3COO)_3 \cdot 4H_2O$ and $Mn(CH_3COO)_2 \cdot H_2O$ were added to 100 ml of 1,4-butanediol, and the mixture was set in a 300 ml-autoclave. After replacement of the atmosphere in the autoclave with nitrogen, the mixture was heated to 300 °C at a rate of 2.3 °C/min and kept at that temperature for 2 h. After cooling, the resulting powder product was collected by centrifugation. They were washed with acetone, air-dried, and then calcined at 400 °C for 4 h in air.

Barium oxide was loaded on Ce–Mn(*x*) by an impregnation method using an aqueous solution of barium nitrate, followed by calcination at 800 °C for 1 h. The barium loading (as BaO) was adjusted to 7 wt% [34]. These catalysts were designated as BaO/Ce–Mn(*x*). The BaO-loaded CeO_2 (BaO/Ce–Mn(0)) and Mn_2O_3 (BaO/Ce–Mn(1.0)) catalysts were prepared in the similar way.

2.2. Direct NO decomposition

Catalyst performance tests for NO decomposition were carried out in a fixed-bed flow reactor of quartz glass tubing with an inner diameter of 10 mm. The catalyst (0.50 g), after pressed into a pellet and pulverized into 10–22 mesh size, was placed in the reactor. The catalyst bed was heated to 550 °C in a helium flow and held at that temperature for 30 min. Then, the reaction gas composed of 6,000 ppm NO and helium balance was introduced to the catalyst bed at 30 ml/min (W/F = 1.0 g·s·ml^{-1}, SV ≈ 5,000 h^{-1}). The reaction temperature was increased from 550 to 800 °C at 5 °C/min and kept for 15 min at every 50 °C interval to attain the stationary state. The effluent gas was analyzed using a gas chromatograph (GL Science, MicroGC 2002) equipped with Molsieve 5A and Poraplot Q columns. The NO conversion is expressed on the basis of the formation of N_2:

$$\text{NO conversion} = \frac{2[N_2]_{out}}{[NO]_{in}},$$

where $[N_2]_{out}$ is the N_2 concentration in the exhaust and $[NO]_{in}$, the NO concentration in the feed.

In the present study, only small amounts of the by-product, N_2O (< 50 ppm), were observed for all the catalysts tested.

2.3. Characterization of the catalysts

Powder X-ray diffraction (XRD) patterns were recorded on a Shimadzu XD-D1 diffractometer using CuKα radiation and a carbon-monochromator. The crystallite size was calculated from the half-height width of the diffraction peak using the Scherrer equation.

The specific surface areas of the samples were calculated by the BET single-point method on the basis of the nitrogen uptake measured at 77 K using a Micromeritics Flowsorb II 2300 sorptograph.

Raman spectra were recorded on a Jobin-Yvon T64000 Raman spectrometer at room temperature using a 514.5 nm argon laser beam.

The reduction behavior of the catalyst was examined by temperature-programmed reduction with H_2 (H_2-TPR) using a flow-type reactor. A portion (100 mg) of the sample was set in the reactor, and it was activated at 300 °C for 30 min in an Ar flow followed by cooling to room temperature. Then, 2 vol. % of H_2 with Ar balance was passed through the catalyst under atmospheric pressure with a flow rate of 30 ml/min. The catalyst was heated to 900 °C at a rate of 5 °C/min, while the amount of H_2 consumed was monitored with a thermal conductivity detector of a Shimadzu 4CPT gas chromatograph.

Electron spin resonance (ESR) spectra were recorded with a JES-SRE2X

spectrometer (JEOL) at room temperature. The *g*-factor was determined by using an Mn^{2+} marker doped in MgO.

X-Ray photoelectron spectroscopy (XPS) measurement was performed on an ULVAC-PHI Model 5500 spectrometer with 15 kV, 400 W MgKα emission as the X-ray source. The charging effect was corrected by adjusting the binding energy of the C 1s peak as 284.6 eV.

3. Results

3.1. NO decomposition activity of BaO/Ce–Mn(x)

The effect of the Mn/(Ce+Mn) ratio on the NO conversion at various temperatures is shown in Fig. 1. The BaO/Ce–Mn(1.0) catalyst exhibited only quite low NO conversions (3% at 700 °C and 7% at 800 °C), whereas BaO/Ce–Mn(0) showed slightly higher NO conversions (7% at 700 °C and 18% at 800 °C). On the other hand, by the use of Ce–Mn mixed oxides as the supports, the catalysts attained significantly enhanced NO conversions. The highest NO decomposition activity was obtained at x = 0.25; 68% NO conversion to N_2 was attained at 800 °C.

<Fig. 1>

3.2. Physical properties of Ce–Mn(x) and BaO/Ce–Mn(x)

Fig. 2 shows the XRD patterns of Ce–Mn(*x*) calcined at 400 ºC for 4 h. All the Ce–Mn(*x*) samples except for the MnO_x sample (Ce–Mn(1.0)) exhibited diffraction peaks at 2θ = 28.3°, 33.1°, 47.5°, 56.5°, and 69.4°, and these peaks are attributed to CeO_2 with a cubic fluorite structure (JCPDS #34-0394). For the samples with low Mn contents, no diffraction peaks due to Mn-containing phases were observed, and for Ce–Mn(*x*) with $x \geq 0.5$, diffraction peaks due to manganese oxides, MnO (JCPDS #07-0230), Mn_2O_3 (JCPDS #41-1442) and Mn_5O_8 (JCPDS #39-1218), were detected in addition to the CeO_2 peaks. Since the glycothermal conditions are severely reducing ones [35–37], MnO was formed. Imamura et al. [38] reported that the addition of a small amount of cerium ions to manganese oxide remarkably affected its oxidation state. The diffraction pattern of a physical mixture of CeO_2 (Ce–Mn(0)) and Mn_2O_3 (Ce–Mn(1.0)) (mixed after calcination of both at 400 ºC) with the Mn/(Ce+Mn) ratio of 0.5 is also shown in Fig. 2a. As compared with the intensities of the peaks observed in this mixture, the intensities of the peaks due to Mn oxides in Ce–Mn(0.5) are apparently small (Fig. 2e), suggesting that the major part of the Mn species is highly dispersed in the Ce–Mn(*x*) samples. With increasing *x*, the intensities of the peaks due to the fluorite

phase decreased and the peaks shifted toward the higher angle side. The latter result indicates that Mn ions are partly incorporated in the fluorite structure. The solubility limit of Mn ions in the CeO_2 lattice was reported to be 50% [31,33], which is consistent with the results shown in Fig. 2.

<Fig. 2>

The XRD patterns of BaO/Ce–Mn(*x*) are shown in Fig. 3. For the catalysts with higher Mn contents, diffraction peaks due to Mn_2O_3 and $BaMnO_{3-\delta}$ (JCPDS #26-0170) were observed. However, the peaks due to other manganese oxide phases detected in the catalyst supports (Fig. 2) disappeared by calcination at 800 ºC. For BaO/Ce–Mn(0.2), and BaO/Ce–Mn(0.25), a trace of $BaMnO_{3-\delta}$ was crystallized but no other Mn oxide phases were detected, suggesting the incorporation of the major part of Mn ions in the fluorite structure.

<Fig. 3>

Impregnation of Ce–Mn(*x*) with $Ba(NO_3)_2$ and subsequent calcination at 800 °C

caused the shift of the CeO_2 diffraction peaks toward the lower angle side, indicating that Ba ions are also incorporated into the cubic fluorite structure. The CeO_2 sample (BaO/Ce–Mn(0)) exhibited small peaks due to $BaCeO_3$ (JCPDS #22-74), which was reported to be formed by calcination of mixtures of BaO and CeO_2 at >800 ºC [39,40]. However, this phase was not detected in the other BaO/Ce–Mn(*x*) samples. In Table 1, physical properties of Ce–Mn(*x*) and BaO/Ce–Mn(*x*) are summarized. The BET surface area of the catalyst decreased with the increase in the Mn content.

<Table 1>

3.3. ESR spectra of Ce–Mn(x) and BaO/Ce–Mn(x)

Fig. 4 shows the ESR spectra of Ce–Mn(*x*) calcined at 400 °C and BaO/Ce–Mn(*x*), and ESR parameters of these samples are summarized in Table 2. The isolated Mn^{2+} ion gives six hyperfine lines with a *g*-factor around 2.0 with a hyperfine coupling constant, *A*, in a range of 8–10 mT. On the other hand, Mn^{4+} gives a *g*-value lower than 2 with an *A* value around 7.6 mT, while Mn^{3+} is ESR silent [41]. All the spectra shown in Fig. 4 exhibited six hyperfine lines with *g*-factors centered at 2.0 and an average *A* value of approximately 9 mT, indicating the presence of Mn^{2+} in the CeO_2 lattice. With the

increase in *x*, the intensity of the ESR signals for the Ce–Mn(*x*) samples (Fig. 4A) increased up to $x = 0.25$, but further increase in *x* decreased the intensity. This feature was also observed for the Ce–Mn(*x*) samples calcined at 800 °C (data not shown). These results are in accordance with the findings reported by Murugan and Ramaswamy [44]. They prepared $Mn/CeO_2–TiO_2$ solid solutions, and found a steep increase in the intensity of the ESR signals due to isolated Mn^{2+} ions up to a concentration of 10 mol% of Mn, above which (≥ 20 mol%) the intensity of the sextet pattern decreased. For the excess Mn ions that did not give the sextet pattern, they suggested two possibilities, i.e., formation of clustered Mn^{2+} species and presence as Mn^{3+} species.

<Fig. 4>

<Table 2>

As shown in Fig. 4B, the intensities of the ESR signals of the BaO/Ce–Mn(*x*) catalysts with $0.25 \leq x \leq 0.75$ were essentially constant, indicating that the proportion of Mn^{2+} in these catalysts decreased with increasing *x*. This result accords with the results of H_2-TPR and XPS analyses described later (Tables 3 and 4).

3.4. H_2-TPR analysis of Ce–Mn(x) and BaO/Ce–Mn(x)

Figs. 5A and 5B show the H_2-TPR profiles of Ce–Mn(*x*) and BaO/Ce–MnO(*x*) both calcined at 800 °C, together with that of a commercial Mn_2O_3 sample (Fig. 5B(a)). The commercial Mn_2O_3 exhibited two reduction peaks at around 350 and 480 °C. Tang et al. [45] observed two-step reduction in the H_2-TPR profile of Mn_2O_3, and they assigned the low-temperature peak to the reduction of Mn_2O_3 to Mn_3O_4 and the high-temperature peak to the further reduction of Mn_3O_4 to MnO. The reduction peaks of the Ce–Mn(1.0) sample were observed at slightly lower temperatures (Fig. 5A(a)) than those observed for commercial Mn_2O_3. With decreasing the Mn content, the reduction peaks shifted to lower temperature side and peak area became small. The H_2-TPR analyses of the Ce–Mn mixed-oxide system (calcined at 350–550 °C) have been done by some researchers [31,45,46]. They suggested that the reduction peak at a low temperature corresponded to the reduction of manganese oxide species (MnO_2 and/or Mn_2O_3), while the high-temperature reduction peak was attributed to the combined reductions of Mn_3O_4 and surface Ce species. In the present study, pure CeO_2 calcined at 400 (Fig. 5A(g)), 600 (Fig.. 5A(f)), and 800 °C (Fig.. 5A(e)) showed two reduction peaks at <600 °C and >800 ºC, and these peaks can be attributed to the surface and bulk reduction of CeO_2 particles, respectively [44–48]. With increasing the calcination

temperature, the reduction peak at low temperature shifted to higher temperature side and the peak area decreased (Figs. 5A(e), (f), and (g)). The reduction temperature of the pure CeO_2 sample calcined at 800 ºC (Fig. 5A(e)) was much higher than those observed for the Ce–Mn(x) ($x \neq 0$) samples, and the peak area for the former sample was negligibly small. From these results, the reduction peaks in the H_2-TPR profiles of Ce–Mn(x) ($x \neq 0$) were attributed exclusively to the reduction from Mn^{3+} to Mn^{2+}.

<Fig. 5>

For the BaO-loaded samples, the reduction peaks further shifted to lower temperatures, indicating the redox property of the Mn species was affected by Ba addition (Figs. 5B(b), (c), (d), and (e)). Comparison between Ce–Mn(0.75) and BaO/Ce–Mn(0.75) (Figs. 5A(b) and 5B(c)) showed that Ba loading caused a slight decrease in the intensity of the low-temperature peak. For both the series of the samples with lower Mn contents, the low-temperature peak vanished and a broad reduction peak was observed at around 300–400 °C. Two other significant changes were observed by decreasing the Mn content; the onset temperature of the reduction increased, and the peak area decreased significantly. These results suggest that the Mn ions in the samples

with the Mn content lower than 0.5 are in a state different from those in the MnO_x phases.

The amounts of hydrogen consumed in the TPR experiments are summarized in Table 3. For Ce–Mn(1.0), the H_2 consumption was 6.18 mmol/g, which almost corresponds to the value calculated for the reduction of Mn_2O_3 to MnO (6.31 mmol/g). For the sample with *x* of 0.75, H_2 consumption was 3.1 mmol/g. This value was 84% of the theoretical, indicating that 16% of the Mn species in the sample was present as Mn^{2+}. With decreasing the Mn content, the proportion of Mn^{2+} in the sample increased. A similar trend was also observed for the samples with Ba loading (Table 3).

<Table 3>

3.5. XPS spectra of Ce–Mn(x) and BaO/Ce–Mn(x)

Fig. 6 shows the XPS of the BaO/Ce–Mn(*x*) catalysts in the Mn 2p region. All the samples exhibited the Mn $2p_{3/2}$ and Mn $2p_{1/2}$ peaks at around 640.5 and 652.5 eV, with a shoulder peak at around 656.1 eV. The shoulder peak became significant with decreasing the Mn content and was attributed to the Ba(MNN) Auger peak [49]. However, the XPS spectra of the reference samples of Mn_3O_4 and MnO_2 exhibited the

$Mn2p_{3/2}$ peak at around 641.2 and 642.3 eV, respectively (data not shown), indicating that the average valence of the Mn species in the present samples was lower than those of the Mn reference samples. This result is in consistent with the result obtained from the H_2-TPR (Table 3); Mn^{2+} was present in the samples. As Fig. 6 shows, the peaks were deconvoluted to Mn components and Ba(MNN) component. The Mn $2p_{3/2}$ peaks of all the samples can be deconvoluted to two peaks at binding energies of ~640 and ~641 eV. This result suggests that the Mn species of all the Ba-loaded samples are in +2 and +3 oxidation states. Qi and Yang reported [32] that the Mn $2p_{3/2}$ peaks in MnO_x–CeO_2 mixed oxide (Mn/(Mn+Ce) = 0.3) were at higher binding energies (around 640.7, 642.3, and 644.5 eV for Mn^{2+}, Mn^{3+}, and Mn^{4+} species) than those for pure Mn oxides (640.9, 641.7, and 642.5 eV for MnO, Mn_2O_3, and MnO_2). However, the Mn $2p_{3/2}$ peak due to Mn^{2+} of the present samples (actually the samples of Qi and Yang as well) were observed at apparently lower binding energy position, presumably because of accommodation of Mn^{2+} ions in the CeO_2 matrix.

<Fig. 6>

Table 4 shows the XPS results for the Ce–Mn(*x*) samples (without Ba) calcined at

400 ºC and BaO/Ce–Mn(*x*) catalysts calcined at 800 ºC. For the BaO-loaded samples, the proportions of Mn^{2+} calculated from the XPS spectra are in reasonable agreement with the values calculated from the TPR profiles, and both results suggest that the Mn^{2+} proportion in the Mn species increased with decreasing the Mn content as depicted in Fig. 7.

Although the BaO/Ce–Mn(*x*) catalysts had higher Mn^{2+} proportions as compared with the corresponding Ce–Mn(*x*) samples, this is because the BaO/Ce–Mn(*x*) catalysts were calcined at higher temperature, and the Ce–Mn(0.25) sample calcined at 800 ºC had the Mn^{2+} proportion essential identical with that of the BaO/Ce–Mn(0.25) catalyst.

<Fig. 7>

Table 4 also shows that the Ce–Mn(*x*) samples had Ce-rich surface compositions. However, the BaO/Ce–Mn(*x*) catalysts with low Mn contents (x = 0.1, 0.2, and 0.25) had Mn-rich surface compositions, whereas those with high Mn contents (x = 0.5, and 0.75) had Ce-rich surface compositions, indicating that a large amount of Mn is present inside the particles.

<Table 4>

3.6. Raman spectra of Ce–Mn(x) and BaO/Ce–Mn(x)

The Raman spectra of CeO_2 and BaO/Ce–Mn(x) catalysts both calcined at 800 °C are shown in Fig. 8A. The Raman peak due to CeO_2 was observed at 463.7 cm^{-1}. This result is consistent with the report that CeO_2 exhibits a characteristic Raman peak at 462–466 cm^{-1} due to the F_{2g} active mode [50,51]. For the BaO/Ce–Mn(0) (BaO/CeO_2) (Fig. 8A(g)) sample, the Raman spectrum was similar to that of CeO_2. However, for the Mn-containing samples ($x > 0$), the Raman peak was observed at ~456.6 cm^{-1}, a significantly lower wavenumber than that observed for the pure CeO_2 sample: Broadening of the peak was also observed.

<Fig. 8>

The peak shift as well as the broadening of the peak was also observed for the Ce–Mn samples (without BaO) calcined at 400 °C (Fig. 8B), indicating that the shift and broadening of the F_{2g} peak of CeO_2 were brought about by the incorporation of Mn ions in the CeO_2 matrix.

In addition to the peak due to CeO_2, Ce–Mn(x) ($x \geq 0.5$) calcined at 400 °C had a Raman peak at 648.5 cm^{-1} (Fig. 8B), which was attributed to that of the Mn_5O_8 phase detected by XRD. A relatively sharp peak at 262.2 cm^{-1} and other low-intensity peaks observed for the Ce–Mn(0.75) sample are also due to this phase [52,53]. Since MnO [54,55] and Mn_2O_3 (Fig. 8C) exhibit relatively weak Raman bands, these phases were not detected by the present Raman spectra. For BaO/Ce–Mn(x) ($x > 0$), a weak peak was observed at 653.3 cm^{-1}, which can be attributed to the Mn_3O_4 phase (Mn_3O_4 exhibited a peak at 654.8 cm^{-1} as shown in Fig. 8C). This phase was not detected by the XRD analysis (Fig. 3), suggesting that it was highly dispersed on the catalyst surface. The Ce–Mn(x) samples calcined at 800 °C (without Ba) exhibited a Raman peak at 652.5 cm^{-1} (data not shown), indicating that the Mn_3O_4 phase was formed by thermal treatment. It was found that the BaO/Ce–Mn(x) sample exhibited higher intensity Raman peak due to Mn_3O_4 than the corresponding Ce–Mn(x) sample calcined at 800 °C (data not shown), indicating that Ba loading facilitates the formation of Mn_3O_4 phase. For the BaO/Ce–Mn(0.8) and BaO/Ce–Mn(0.75) samples, a Raman peak with a very low intensity was observed at 312.4 cm^{-1}, which is due to the Mn_2O_3 phase detected by the XRD technique. Mn_2O_3 exhibited a low intensity peak at 312.4 cm^{-1} as shown in Fig. 8C.

Substitution of a part of Ce ions with Mn ions would cause the formation of oxygen vacancies straining the CeO_2 structure. For all the samples, broad Raman peaks were also observed at ~256 and ~582 cm^{-1} (Fig. 8A), which are attributed to the defect space including an O^{2-} vacancy [56]. However, the peak at ~582 cm^{-1} may overlap with the peak due to the Mn species, because the intensity of this peak increased with increasing the Mn content. Consequently, the Raman peak at ~256 cm^{-1} of the BaO/Ce–Mn(*x*) catalysts (shaded peak in Fig. 8A) is attributed exclusively to the oxygen vacancy. The intensity ratio of the peak at ~256 to that at ~456 cm^{-1} (denoted as I_{256}/I_{456}) indicates the relative concentration of oxygen vacancies in the solid solution. Fig. 9 shows the effects of the Mn content on the I_{256}/I_{456} values for BaO/Ce–Mn(*x*). For comparison, the NO conversions (at 800 °C) on the BaO/Ce–Mn(*x*) catalysts are also plotted in the figure. The concentration of the oxygen vacancies increased with increasing *x*, and the highest I_{256}/I_{456} value was attained for $x = 0.25$; further increase in the Mn content decreased the concentration of oxygen vacancies. The I_{256}/I_{456} profile for the BaO/Ce–Mn(*x*) catalyst is similar to that of its NO decomposition activity; the highest NO conversion was attained with BaO/Ce–Mn(0.25) having the highest I_{256}/I_{456} value, suggesting that oxygen vacancy plays an important role in this reaction.

<Fig. 9>

For the Ce–Mn(x) samples without Ba loading, a similar I_{256}/I_{456} profile was obtained. The Ce–Mn(x) samples with the x value of 0.2–0.5 had the I_{256}/I_{456} values of ~0.05, higher than those observed for the corresponding BaO/Ce–Mn(x) catalysts, indicating that Ba loading decreased the concentration of oxygen vacancies in the solid solution. For the Ce–Mn(x) samples with high x values, however, the I_{256}/I_{456} values could not be determined because the Raman peak at ~256 cm^{-1} partly overlapped with the peak at 262.2 cm^{-1} due to the Mn_5O_8 phase.

4. Discussion

Since Mn^{2+} has an ionic radius (96 pm [57]) similar to that of the host Ce^{4+} (114 pm [57]), it can occupy the Ce^{4+} sites by isomorphous substitution. However, Mn^{3+} seems to occupy defect sites or surface sites of CeO_2 crystals, because it has a much smaller ionic radius (58 pm [57]). When a Ce^{4+} ion is substituted with a Mn^{2+} ion, an oxygen vacancy is formed to maintain the charge balance, while Mn^{3+} ions in defect or surface sites cause the disappearance of oxygen vacancies and/or formation of extra oxide ions. When Ce–Mn(x) with a low x value was prepared, Mn^{2+} ions selectively occupy the

Ce^{4+} sites. Substitution of Ce^{4+} ion with Mn^{2+} ions, causing the formation of oxygen vacancies, makes the lattice unstable; therefore, a limited concentration of Mn^{2+} ions can be accommodated in the Ce^{4+} sites of the CeO_2 lattice. Further increase in *x* value promotes the formation of Mn^{3+} ions in defect or surface sites, and decreases the concentration of oxygen vacancies (Fig. 9). This scenario accords with the data presented in this paper. The Mn^{2+} content in the solid solution, as observed by ESR signals, were essentially constant irrespective of the *x* value. The Mn^{2+} proportion in Mn species, as calculated from H_2-TPR profiles and XPS spectra, decreased with the increase in the *x* value. The lattice constant slightly decrease with the increase in the *x* value, but Ce–Mn(*x*) samples with large *x* values had the unit cell parameter essentially identical with that of pure CeO_2 (Table 1). This is because an excess Mn content caused incorporation of a number of Mn^{3+} ions in the defect sites of CeO_2, which would expand the unit cell parameter. This effect compensates the lattice shrinkage effect of Mn^{2+} ions incorporated in the Ce^{4+} sites.

Now the effect of Ba loading on the physical properties of the catalysts is discussed. The following results were obtained: (1) Unit cell of the fluorite lattice was significantly expanded (Table 1). (2) Ba loading decreased the concentration of oxygen vacancies caused by incorporation of Mn^{2+} ions in the fluorite lattice (Fig. 8). (3) Ba loading

significantly decreased the ESR signals due to isolated Mn^{2+} species (Fig. 4). (4) Ba loading facilitated the reduction of Mn^{3+} species in the catalyst (Fig. 5). (5) When estimated from the H_2-TPR profile (Table 3), the Mn^{2+} proportion in the Mn species was not altered by Ba loading (Although Table 4 shows that the Mn^{2+} proportion increased by Ba loading, this result is caused by the difference in calcination temperature). (6) For the samples with low Mn contents, Mn concentration in the surface region increased by Ba loading (Table 4). These results suggest the following scenario. The Ba loading and subsequent calcination at 800 °C cause diffusion of a part of Ba ions into CeO_2 and accommodation of them in the interstitial sites of the fluorite lattice, which is supported by the significant increase in the lattice parameter (Table 1). Substitution of Ce^{4+} ions with Ba^{2+} ions would not take place because this process requires the diffusion of tetravalent cerium cations. The decrease in the concentration of oxygen vacancies in the BaO/Ce–Mn(*x*) catalysts as compared with the corresponding Ce–Mn(*x*) samples supports this argument. The marked decrease in the intensities of the ESR signals due to isolated Mn^{2+} ions by Ba loading suggests that a part of the Mn^{2+} ions diffused out from the fluorite lattice; only the Mn^{2+} ions remaining in the Ce sites give the ESR hyperfine signals. The growth of the fluorite crystallites by calcination at a high temperature expels the Mn^{3+} ions in the defect sites to outer surface of the crystallites, which was

supported by the increase in surface Mn content by Ba loading and subsequent calcination. The facile reduction of Mn^{3+} species in the BaO/Ce–Mn(*x*) samples may be due to the location of Mn^{3+} species.

The NO conversions at 600 ºC (The data at this reaction temperature were taken because NO conversions were relatively low) were divided by concentration of oxygen vacancies (I_{256}/I_{456} value), and the results are shown in Fig. 9. Since the data should be proportional to the NO decomposition activity normalized by the amount of oxygen vacancies, like TOF, the calculated value was essentially constant in the range of Mn/(Ce+Mn) < 0.5. The large increase in the calculated value in the region $x > 0.5$ seems to be due to the underestimation of the concentration of oxygen vacancies.

The TOF values were calculated assuming that all the Mn^{2+} species contributed the formation of oxygen vacancies, and that the catalyst exposes 111 surface of the fluorite structure where the highest density of Ce ions per unit surface area is expected. The calculated TOF values for BaO/Ce–Mn(0.1), BaO/Ce–Mn(0.2), and BaO/Ce–Mn(0.25) catalysts were 2.3×10^{-3}, 1.4×10^{-3}, and 1.7×10^{-3} s^{-1} (at 600 ºC), respectively. The order of magnitude of these values is within the range of that of the TOF values reported for Pd catalyzed decomposition of NO ($1–13 \times 10^{-2}$ s^{-1} for 1–20 wt% Pd/BeO at 700 ºC [58]; $2–3 \times 10^{-3}$ s^{-1} for 1–20 wt% Pd/SiO_2 at 700 ºC [58]; 1.6×10^{-4} s^{-1} for 5 wt%

Pd/Al_2O_3 at 500 ºC [3]). However, the calculated TOF is only rough estimation, because Mn^{3+} ions in defect or surface sites as well as Ba^{2+} ions in the interstitial sites of the fluorite lattice decrease the concentration of oxygen vacancies.

In the previous work [34], we examined the NO decomposition activities of Ce–Mn mixed oxides modified with alkali and alkaline earth elements and found that the NO decomposition activities of the catalysts are correlated well with their basic properties. The addition of Ba to Ce–Mn mixed oxides produced considerably strong NO adsorption sites on the surface. It was reported that NO_x species adsorbed on BaO have mobility (spillover) to other catalyst components [59,60]. Therefore, one possible explanation for the role of Mn^{2+} ions is that NO species adsorbed on the BaO sites migrate to oxygen vacancies of the Ce–Mn solid solution, where NO is decomposed. Similar bifunctional mechanisms have been proposed for many catalytic systems; for examples, Zhang et al. concluded that in catalytic reduction of NO by CO over $Cu/Ce_xZr_{1-x}O_2$, NO is adsorbed on Cu^+ sites while intermediate N_2O is reduced on Ce^{3+} sites associated with oxygen vacancies [61]. Incorporation of Mn^{2+} in the fluorite structure of CeO_2 ($x < 0.5$) causes an increase in the concentration of oxygen vacancies, which play important roles to derive the NO decomposition activity. This argument is supported by the report that the oxygen vacancies in the catalysts played an important

role in NO dissociation [11,16–18].

5. Conclusions

Direct NO decomposition activities of BaO catalysts supported on Ce–Mn mixed oxide with various Mn contents were examined and the highest activity was obtained for the sample with $x = 0.25$ (x = Mn/(Ce+Mn) mole ratio). The XRD and Raman results indicated that the Ce–Mn(x) solid solutions with a cubic fluorite structure were formed. The ESR spectra showed that isolated Mn^{2+} species were present in the BaO/Ce–Mn(x) catalysts. Incorporation of Mn^{2+} in the fluorite structure of CeO_2 causes an increase in the concentration of oxygen vacancies, which play important roles in the NO decomposition activity. The H_2-TPR profiles and XPS spectra indicated that Mn^{2+} proportion in the Mn species increased with decreasing the Mn content, suggesting that a limited concentration of Mn^{2+} ions can be accommodated in the Ce^{4+} sites of the CeO_2 lattice, and the BaO/Ce–Mn(0.25) catalysts showed the highest NO decomposition activity. Further increase in the Mn content causes the formation of Mn^{3+} ions in defect sites or surface sites, and decreases the concentration of oxygen vacancies, thus decreasing the NO decomposition activity of the catalysts.

Acknowledgements

This work was supported by a Grant-in-Aid from Ministry of Education, Culture, Sports, Science and Technology, Japan.

We thanks Prof. Takeshi Abe of Kyoto University for his help in Raman spectra measurements and Dr. Seiichiro Imamura for his invaluable advice.

One of the authors (W.-J. H.) thanks Prof. Misook Kang of Yeungnam University for her discussions.

References

[1] A. Amirnazmi, J.E. Benson, M. Boudart, J. Catal. 30 (1973) 55.

[2] R.J. Wu, T.Y. Chou, C.T. Yeh, Appl. Catal. B: Environ. 6 (1995) 105.

[3] M. Haneda, Y. Kintaichi, I. Nakamura, T. Fujitani, H. Hamada, J. Catal. 218 (2003) 405.

[4] D.D. Miller, S.S.C. Chuang, J. Phys. Chem. C 113 (2009) 14963.

[5] M. Iwamoto, H. Yahiro, Y. Mine, S. Kagawa, Chem. Lett. 18 (1989) 213.

[6] M. Iwamoto, H. Hamada, Catal. Today 10 (1991) 57.

[7] M.H. Groothaert, J.A. van Bokhoven, A.A. Battiston, B.M. Weckhuysen, R.A. Schoonheydt, J. Am. Chem. Soc. 125 (2003) 7629.

[8] G. Moretti, G. Ferraris, G. Fierro, M. Lo Jacono, S. Morpurgo, M. Faticanti, J. Catal. 232 (2005) 476.

[9] A.M. de Oliveira, I. Costilla, C. Gigola, I.M. Baibich, V.T. da Silva, S.B.C. Pergher, Catal. Lett. 136 (2010) 185.

[10] E.R.S. Winter, J. Catal. 22 (1971) 158.

[11] S.J. Huang, A.B. Walters, M.A. Vannice, J. Catal. 192 (2000) 29.

[12] P.W. Park, J.K. Kil, H.H. Kung, M.C. Kung, Catal. Today 42 (1998) 51.

[13] S.B. Xie, M.P. Rosynek, J.H. Lunsford, J. Catal. 188 (1999) 24.

[14] M. Haneda, Y. Kintaichi, H. Hamada, Appl. Catal. B: Environ. 55 (2005) 169.

[15] Y. Teraoka, H. Fukuda, S. Kagawa, Chem. Lett. 19 (1990) 1.

[16] Y. Teraoka, T. Harada, S. J. Kagawa, J. Chem. Soc., Faraday Trans. 94 (1998) 1887.

[17] T. Ishihara, M. Ando, K. Sada, K. Takiishi, K. Yamada, H. Nishiguchi, Y. Takita, J. Catal. 220 (2003) 104.

[18] H. Iwakuni, Y. Shinmyou, H. Yano, H. Matsumoto, T. Ishihara, Appl. Catal. B: Environ. 74 (2007) 299.

[19] J.J. Zhu, D.H. Xiao, J. Li, X.G. Yang, Y. Wu, J. Mol. Catal. A. Chem. 234 (2005) 99.

[20] J.J. Zhu, A. Thomas, Appl. Catal. B: Environ. 92 (2009) 225.

[21] N. Imanaka, T. Masui, H. Masaki, Adv. Mater. 19 (2007) 3660.

[22] H. Masaki, T. Masui, N. Imanaka, J. Alloys Compd. 451 (2008) 406.

[23] K. Goto, H. Matsumoto, T. Ishihara, Top. Catal. 52 (2009) 1776.

[24] S. Iwamoto, T. Yasuda, M. Inoue, Adv. Technol. Mater. Mater. Proc. J. 4 (2002) 58.

[25] S. Iwamoto, T. Yasuda, Y. Kouno, M. Inoue, Adv. Sci. Technol. 33 (2003) 375.

[26] S. Iwamoto, R. Takahashi, M. Inoue, Appl. Catal. B: Environ. 70 (2007) 146.

[27] W.-J. Hong, S. Iwamoto, M. Inoue, Catal. Lett. 135 (2010) 190.

[28] A. Trovarelli, Catal. Rev.-Sci. Eng. 38 (1996) 439.

[29] T. Rao, M.Q. Shen, L.W. Jia, J.J. Hao, J. Wang, Catal. Commun. 8 (2007) 1743.

[30] X. Tang, Y. Li, X. Huang, Y. Xu, H. Zhu, J. Wang, W. Shen, Appl. Catal. B: Environ. 62 (2006) 265.

[31] H. Chen, A. Sayari, A. Adnot, F. Larachi, Appl. Catal. B: Environ. 32 (2001) 195.

[32] G. Qi, R.T. Yang, R. Chang, Appl. Catal. B: Environ. 51 (2004) 93.

[33] M. Machida, M. Uto, D. Kurogi, T. Kijima, Chem. Mater. 12 (2000) 3158.

[34] W.-J. Hong, S. Iwamoto, M. Inoue, Catal. Today. (2010), doi: 10.1016/j.cattod.2010.10.063.

[35] M. Inoue, Adv. Sci. Technol. 29 (2000) 855.

[36] M. Takahashi, N. Inoue, T. Takeguchi, S. Iwamoto, M. Inoue, T. Watanabe, J. Am. Ceram. Soc. 89 (2006) 2158.

[37] S. Hosokawa, H.J. Jeon, S. Iwamoto, M. Inoue, J. Am. Ceram. Soc. 92 (2009) 2847.

[38] S. Imamura, M. Shono, N. Okamoto, A. Hamada, S. Ishida, Appl. Catal. A: Gen. 142 (1996) 279.

[39] M. Casapu, J.D. Grunwaldt, M. Maciejewski, M. Wittrock, U. Gobel, A. Baiker, Appl. Catal. B: Environ. 63 (2006) 232.

[40] M. Yang, Y.P. Li, J. Wang, M.Q. Shen, J. Catal. 271 (2010) 228.

[41] G. Qi, R.T. Yang, J. Phys. Chem. B. 108 (2004) 15738.

[42] S. Velu, N. Shah, T.M. Jyothi, S. Sivasanker, Microporous Mesoporous Mater. 33 (1999) 61.

[43] E. Saab, S. Aouad, E. Abi-Aad, E. Zhilinskaya, A. Aboukais, Catal. Today 119 (2007) 286.

[44] B. Murugan, A.V. Ramaswamy, J. Phys. Chem. C. 112 (2008) 20429.

[45] X. Tang, J. Chen, Y. Li, Y. Li, Y. Xu, W. Shen, Chem. Eng. J. 118 (2006) 119.

[46] D. Delimaris, T. Ioannides, Appl. Catal. B: Environ. 84 (2008) 303.

[47] H.C. Yao, Y.F.Y. Yao, J. Catal. 86 (1984) 254.

[48] B. Campo, C. Petit, M.A. Volpe, J. Catal. 254 (2008) 71.

[49] Muilenberg GE (1979) Handbook of X-ray photoelectron spectroscopy. Perkin-Elmer Corporation, Minnesota, p 139.

[50] B.M. Reddy, A. Khan, Catal. Surv. Asia 9 (2005) 155.

[51] F. Arena, G. Trunfio, J. Negro, B. Fazio, L. Spadaro, Chem. Mater. 19 (2007) 2269.

[52] T. Gao, P. Norby, F. Krumeich, H. Okamoto, R. Nesper, H. Fjellvag, J. Phys. Chem. C. 114 (2010) 922.

[53] T.E. Moore, M. Ellis, P.W. Selwood, J. Am. Chem. Soc. 72 (1950) 856.

[54] F. Kapteijn, A.D. Vanlangeveld, J.A. Moulijn, A. Andreini, M.A. Vuurman, A.M.

Turek, J.M. Jehng, I.E. Wachs, J. Catal. 150 (1994) 94.

[55] M. Ferrandon, J. Carno, S. Jaras, E. Bjornbom, Appl. Catal. A: Gen. 180 (1999) 141.

[56] A. Nakajima, A. Yoshihara, M. Ishigame, Phys. Rev. B. 50 (1994) 13297.

[57] R.D. Shannon, Acta Crystallogr. Set. A, 32 (1976) 751.

[58] S. Naito, M. Iwahashi, I. Kawakami, T. Miyao, Catal. Today 73 (2002) 355.

[59] N.W. Cant, I.O.Y. Liu, M.J. Patterson, J. Catal. 243 (2006) 309.

[60] A. Kumar, M.P. Harold, V. Balakotaiah, J. Catal. 270 (2010) 214.

[61] R.D. Zhang, W.Y. Teoh, R. Amal, B.H. Chen, S. Kaliaguine, J. Catal. 272 (2010) 210.

Figure/Table captions

Table 1. Physical properties of Ce–Mn(*x*) and BaO/Ce–Mn(*x*) catalysts.

Table 2. ESR parameters of Ce–Mn(*x*) and BaO/Ce–Mn(*x*) catalysts.

Table 3. Reduction properties of Ce–Mn(*x*) and BaO/Ce–Mn(*x*) catalysts.

Table 4. XPS results for Ce–Mn(*x*) and BaO/Ce–Mn(*x*) catalysts.

Fig. 1. Effect of the Mn/(Ce+Mn) ratio on NO conversion at various temperatures. Catalyst, 0.50 g; reaction gas, 6,000 ppm NO in He; flow rate, 30 ml/min (W/F = 1.0 $g \cdot s \cdot ml^{-1}$).

Fig. 2. XRD patterns of Ce–Mn(*x*) calcined at 400 °C for 4 h: (a) physical mixture of Ce–Mn(0) and Ce–Mn(1.0) (Ce/(Ce+Mn) = 0.5, mixed after calcination at 400 °C); (b) Ce–Mn(1.0); (c) Ce–Mn(0.8); (d) Ce–Mn(0.75); (e) Ce–Mn(0.5); (f) Ce–Mn(0.25); (g) Ce–Mn(0.2); (h) Ce–Mn(0.1); and (i) Ce–Mn(0).

Fig. 3. XRD patterns of BaO/Ce–Mn(*x*) catalysts calcined at 800 °C for 1 h: (a) BaO/(physical mixture of CeO_2 and Mn_2O_3), (Ce/(Ce+Mn) = 0.5); (b) BaO/Ce–Mn(1.0); (c) BaO/Ce–Mn(0.8); (d) BaO/Ce–Mn(0.75); (e) BaO/Ce–Mn(0.5); (f) BaO/Ce–Mn(0.25); (g) BaO/Ce–Mn(0.2); (h) BaO/ Ce–Mn(0.1); and (i) BaO/Ce–Mn(0).

Fig. 4. ESR spectra of Ce–Mn(*x*) calcined at 400 °C (A) and BaO/Ce–Mn(*x*) catalysts (B): (a) *x* = 0.8; (b) *x* = 0.75; (c) *x* = 0.5; (d) *x* = 0.25; (e) *x* = 0.2; and (f) *x* = 0.1.

Fig. 5. H_2-TPR profiles of Ce–Mn(*x*) and BaO/Ce–Mn(*x*) catalysts both calcined at 800 °C (except for A(f), (g) and B(a)). A: (a) Ce–Mn(1.0); (b) Ce–Mn(0.75); (c) Ce–Mn(0.5); (d) Ce–Mn(0.25); (e) Ce–Mn(0); (f) Ce–Mn(0) calcined at 600 °C and (g) Ce–Mn(0) calcined at 400 °C. B: (a) commercial Mn_2O_3 as-received; (b) BaO/Ce–Mn(1.0); (c) BaO/Ce–Mn(0.75); (d) BaO/Ce–Mn(0.5); (e) BaO/Ce–Mn(0.25) and (f) BaO/Ce–Mn(0).

Fig. 6. Mn2p XPS spectra of the BaO/Ce–Mn(*x*) catalysts: (a) *x* = 0.75; (b) *x* = 0.5; (c) *x* = 0.25; (d) *x* = 0.2; and (e) *x* = 0.1.

Fig. 7. Effect of Mn/(Ce+Mn) ratio on the Mn^{2+} proportion in the Mn species calculated from the H_2-TPR and XPS results of the BaO/Ce–Mn(*x*) catalysts.

Fig. 8. Raman spectra of the BaO/Ce–Mn(*x*) catalysts (A), Ce–Mn(*x*) calcined at 400 °C (B), and Mn references (C): (a) *x* = 0.8; (b) *x* = 0.75; (c) *x* = 0.5; (d) *x* = 0.25; (e) *x* = 0.2, (f) *x* = 0.1; and (g) *x* = 0. Raman spectrum of a single component CeO_2 without Ba (Ce–Mn(0)) calcined at 800 °C is also given in A. The Raman peak at 256 cm^{-1} due to the defect structure of CeO_2 is indicated by shade.

Fig. 9. Effect of the Mn/(Ce+Mn) ratio on I_{256}/I_{456} calculated from the Raman spectrum of the BaO/Ce–Mn(*x*) catalyst. For comparison, NO conversion at 800 °C and the NO conversion (at 600 ºC) normalized by oxygen vacancy (I_{256}/I_{456} value) are also plotted in the figure.

Table 1
Physical properties of Ce–Mn(*x*) and BaO/Ce–Mn(*x*) catalysts.

Sample	Surface area (m^2/g)	Crystallite size[a] (nm)	Lattice parameter (Å)
Ce–Mn(0)[b]	134	7	5.408
Ce–Mn(0.1)[b]	130	10	5.408
Ce–Mn(0.2)[b]	132	7	5.403
Ce–Mn(0.25)[b]	121	7	5.397
Ce–Mn(0.5)[b]	88	9	5.408
Ce–Mn(0.75)[b]	67	8	5.407
Ce–Mn(0.8)[b]	46	6	5.406
Ce–Mn(1.0)[b]	9	–	–
BaO/Ce–Mn(0)	24	32	5.412
BaO/Ce–Mn(0.1)	25	22	5.413
BaO/Ce–Mn(0.2)	28	17	5.413
BaO/Ce–Mn(0.25)	28	19	5.412
BaO/Ce–Mn(0.5)	23	16	5.411
BaO/Ce–Mn(0.75)	22	13	5.405
BaO/Ce–Mn(0.8)	11	11	5.398
BaO/Ce–Mn(1.0)	2	–	–

[a] Calculated from the [200] diffraction peak of the fluorite phase.
[b] Calcined at 400 °C for 4 h.

Table 2

ESR parameters of Ce–Mn(*x*) and BaO/Ce–Mn(*x*) catalysts.

Sample	*g*-factor	*A*[a] (mT)
Ce–Mn(0.2)[b]	2.01	9.32
Ce–Mn(0.25)[b]	2.01	9.30
Ce–Mn(0.5)[b]	2.01	9.33
Ce–Mn(0.75)[b]	2.01	9.21
Ce–Mn(0.8)[b]	2.01	9.25
BaO/Ce–Mn(0.1)	2.01	9.23
BaO/Ce–Mn(0.2)	2.01	9.16
BaO/Ce–Mn(0.25)	2.01	9.18
BaO/Ce–Mn(0.5)	2.01	9.21
BaO/Ce–Mn(0.75)	2.01	9.25
BaO/Ce–Mn(0.8)	2.01	9.23

[a] Hyperfine coupling constant.

[b] Calcined at 400 ºC for 4 h.

Table 3

Reduction properties of Ce–Mn(*x*) and BaO/Ce–Mn(*x*) catalysts.

Sample	H_2 consumption (mmol/g)	Peak temperature (°C)	Reduction degree[a] (%)	Mn^{2+} in total Mn[a] (%)
Ce–Mn(0.1)[b]	0.16	245	60	40
Ce–Mn(0.25)[b]	0.52	389	66	34
Ce–Mn(0.5)[b]	1.65	397	83	17
Ce–Mn(0.75)[b]	3.10	384	84	16
Ce–Mn(1.0)[b]	6.18	442	98	2
BaO/Ce–Mn(0.1)	0.18	278	60	40
BaO/Ce–Mn(0.2)	0.42	325	69	31
BaO/Ce–Mn(0.25)	0.56	348	72	28
BaO/Ce–Mn(0.5)	1.65	360	84	16
BaO/Ce–Mn(0.75)	3.11	365	85	15
BaO/Ce–Mn(1.0)	6.18	407	98	2

[a] Calculated by assuming that the Mn species Mn^{3+} state (Mn_2O_3) were reduced to Mn^{2+}.
[b] Calcined at 800 °C for 1 h.

Table 4

XPS results for Ce–Mn(*x*) and BaO/Ce–Mn(*x*) catalysts.

Sample	$Mn2p_{3/2}$ BE (eV)		Mn^{2+} in total Mn (%)	Surface composition Mn/(Ce+Mn) (%)
	Mn^{2+}	Mn^{3+}		
Ce–Mn(0.2)[a]	640.1	640.7	17	12
Ce–Mn(0.25)[a]	640.1	640.7	16	12
Ce–Mn(0.25)[b]	639.1	640.8	21	21
Ce–Mn(0.5)[a]	639.7	640.9	15	50
Ce–Mn(0.75)[a]	639.5	640.7	14	55
BaO/Ce–Mn(0.1)[b]	639.6	640.7	30	20
BaO/Ce–Mn(0.2)[b]	640.0	641.0	26	27
BaO/Ce–Mn(0.25)[b]	640.1	640.5	22	31
BaO/Ce–Mn(0.5)[b]	639.6	640.8	16	35
BaO/Ce–Mn(0.75)[b]	640.1	641.1	12	58

[a] Calcined at 400 ºC for 4 h.

[b] Calcined at 800 ºC for 1 h.

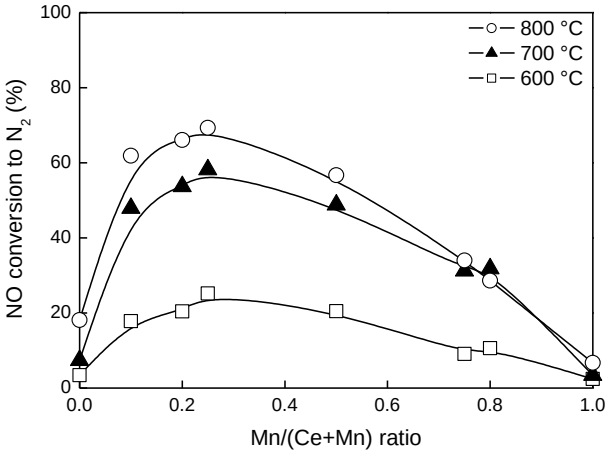

Fig.1. W.-J. Hong et al.

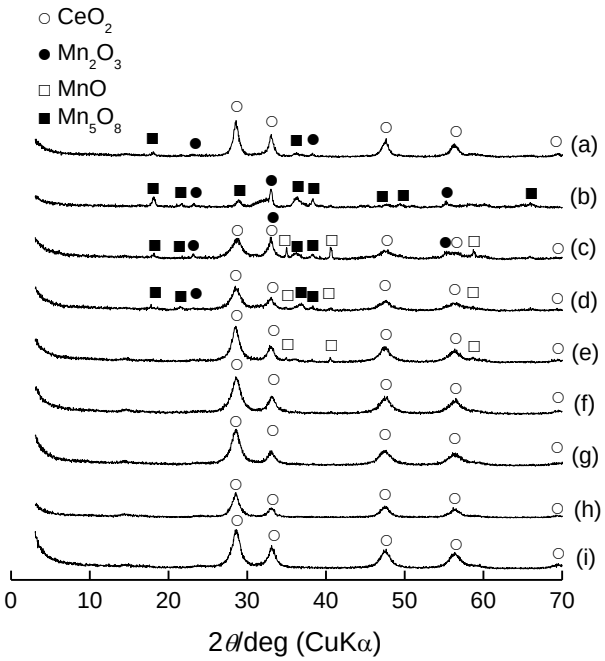

Fig.2. W.-J. Hong et al.

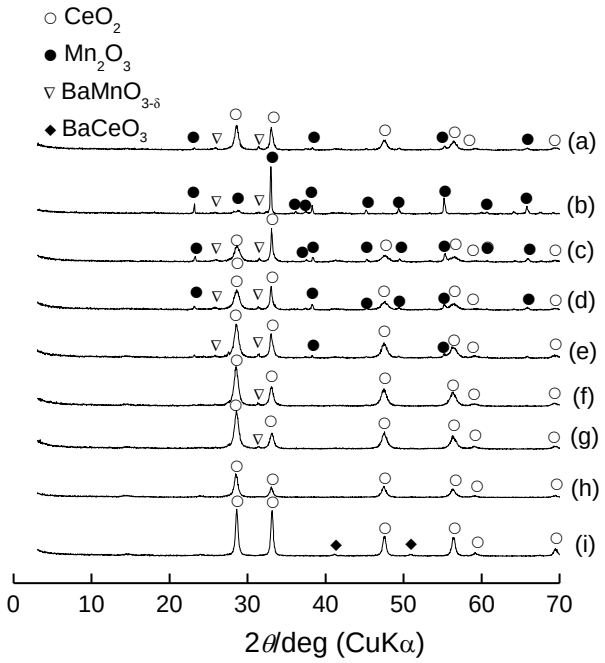

Fig.3. W.-J. Hong et al.

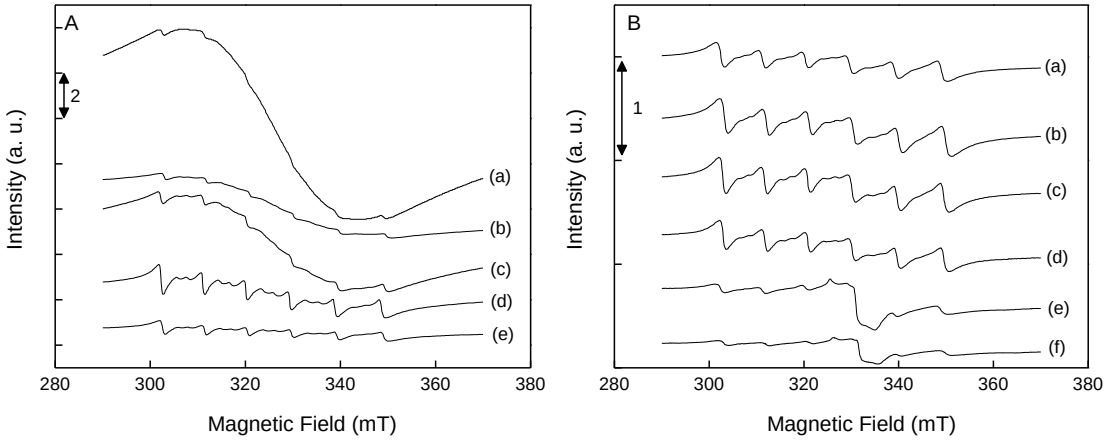

Fig.4. W.-J. Hong et al.

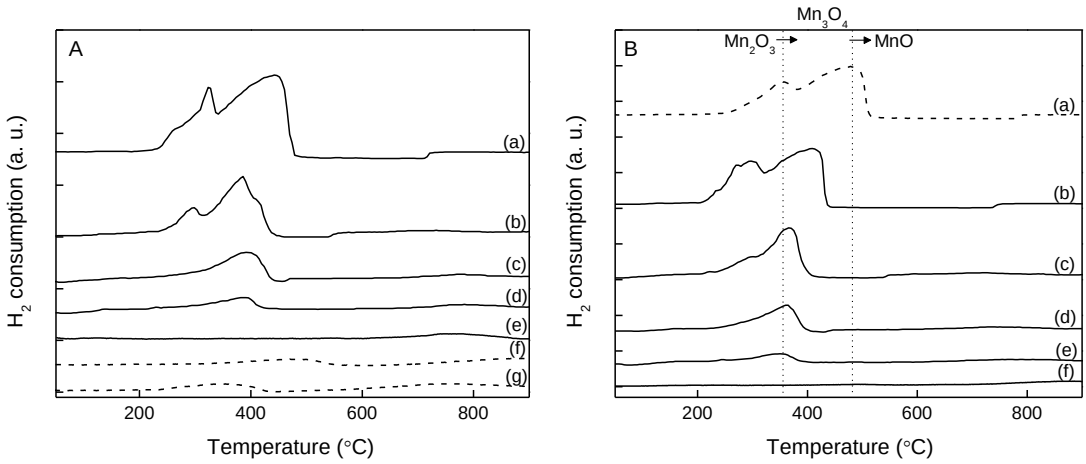

Fig.5. W.-J. Hong et al.

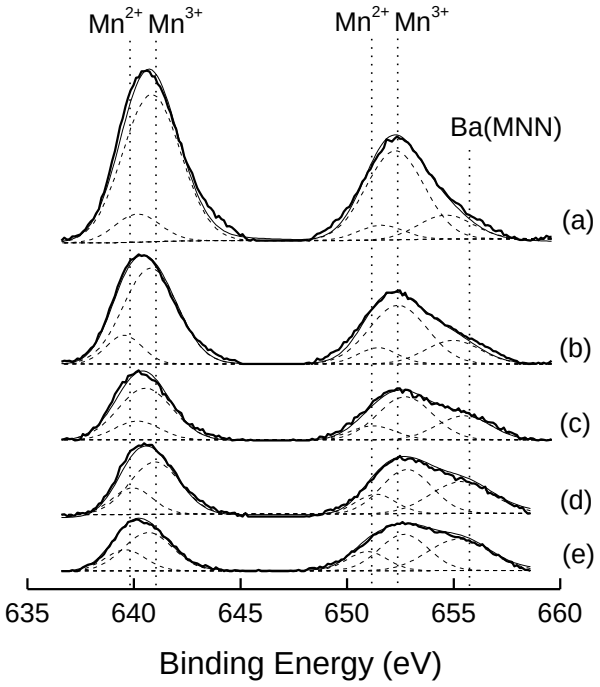

Fig.6. W.-J. Hong et al.

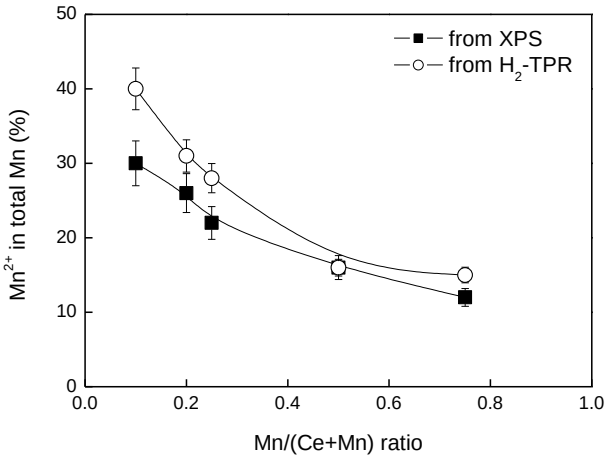

Fig.7. W.-J. Hong et al.

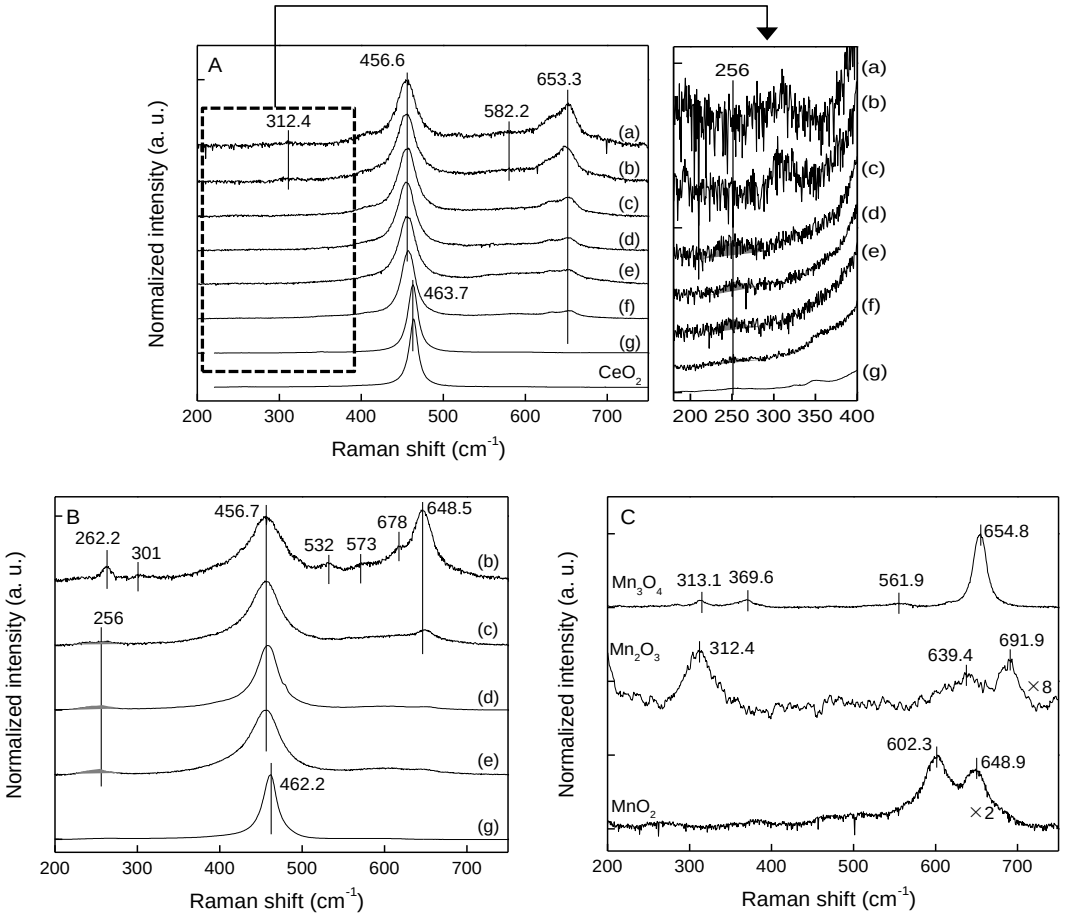

Fig.8. W.-J. Hong et al.

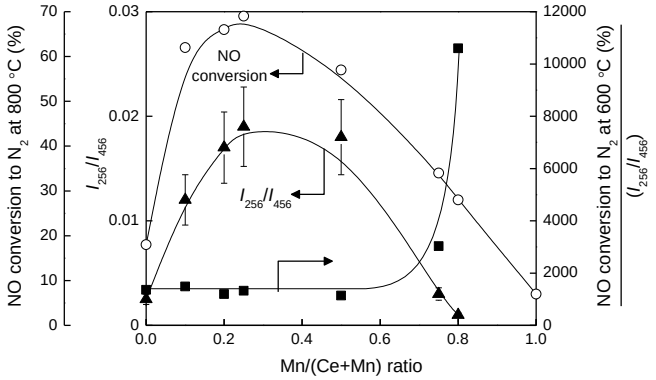

Fig.9. W.-J. Hong et al.